


## RESEARCH ARTICLE

[View Article Online](#)  
[View Journal](#) | [View Issue](#)

 Cite this: *Mater. Chem. Front.*, 2021,  
 5, 1884

# A reinforced ceramic-coated separator by overall-covered modification of electron-insulated polypyrrole for the safe performance of lithium-ion batteries†

 Longqing Peng,<sup>a</sup> Xin Wang,<sup>a</sup> Jianhui Dai,<sup>b</sup> Xiu Shen,<sup>a</sup> Boyang Huang,<sup>a</sup> Peng Zhang\*<sup>b</sup>  
 and Jinbao Zhao <sup>ab</sup>

The safety of lithium-ion batteries (LIBs) is a serious and challenging problem that threatens the applications of large-scale energy storage as well as the daily usage of mobile devices. In this work, we developed a rational design of reinforced ceramic-coated separator by modifying the ceramic-coated separator with an overall-covered layer of electron-insulated polypyrrole throughout the entire separator. As a result, the modified separator shows an improved thermal stability without visible shrinkage at 200 °C, has a better electrolyte wettability and a higher Li<sup>+</sup> transference number of 0.56. With these advantages, cells assembled with the modified separators show better safety performance and an improved rate capability.

 Received 22nd October 2020,  
 Accepted 11th December 2020

DOI: 10.1039/d0qm00849d

[rsc.li/frontiers-materials](http://rsc.li/frontiers-materials)

## 1. Introduction

Thanks to their high energy density, environment-friendliness and excellent cycle stability, lithium-ion batteries (LIBs) have been widely used in mobile communication equipment and digital products.<sup>1,2</sup> With the rapid development of new energy-powered vehicles in recent years, LIBs have been gradually introduced into electric vehicles to solve the serious energy and environmental issues caused by the fossil energy system. However, the frequent spontaneous combustion and explosion accidents of LIBs have severely restricted the rapid development of electric vehicles.

The thermal runaway of batteries is one of the archrivals to the safety of electric vehicles. It is usually triggered by various abused conditions, which lead to a series of exothermic side reactions combined with increasing temperature.<sup>3–5</sup> Separators play a vital role in LIBs. On one hand, they provide Li<sup>+</sup> ion conduction by providing a porous structure and absorbing liquid electrolyte. On the other hand, this ensures the energy conversion as well as the safety of LIBs by preventing the direct contact of cathodes and anodes. However, separators most widely used are polyolefin separators with microporous structures,

which have poor thermal stability and usually show large dimensional shrinkage at elevated temperature.<sup>6,7</sup> As a result, this leads to an internal short circuit of the cell and thermal runaway.<sup>8–10</sup> Moreover, due to nonpolar surface character, polyolefin separators have bad wettability with commercial electrolytes, which not only prolongs the time for assembly in battery manufacturing processes, but also results in poor battery performance.<sup>11–14</sup>

Many measures have been carried out to overcome these problems. One common strategy is to substitute polyolefin with a highly thermal resistant polymer to prepare porous membranes, such as polyimide (PI) and polybenzimidazole (PBI).<sup>13,15</sup> However, the inevitable usage of toxic organic solvents in manufacturing process and high cost impede its further commercialization. The other direction is to cut down or avoid the use of combustible liquid electrolytes, such as the gel polymer electrolyte and all-solid electrolyte.<sup>16–19</sup> However, incomparable performance, such as low ionic conductivity, poor mechanical property and high interface impedance, lead a long way for commercial application.<sup>15,20–25</sup> By comprehensive consideration of the cost, performance and manufacturing process, ceramic-coated separators (CCSs), in which polyolefin separators are modified with a thin coating layer of inorganic particles, are still the most practical way to improve the safety of separators.<sup>26</sup> On one hand, CCS maintains the advantages of the polyolefin separator, such as its low cost and excellent mechanical strength. On the other hand, it not only enhances the thermal stability of separators, but also improves the wettability and retention capacity with the electrolyte.<sup>11,27–29</sup> However, the thermal stability of CCS is still not effective enough due to the poor mechanical strength of the ceramic-coated layer and weak interaction between the polyolefin separator and ceramic particles.

<sup>a</sup> College of Chemistry and Chemical Engineering, Xiamen University, Engineering Research Center of Electrochemical Technology, Ministry of Education, State-Province Joint Engineering Laboratory of Power Source Technology For New Energy Vehicle, Xiamen 361005, China. E-mail: jbzha@xmu.edu.cn

<sup>b</sup> College of Energy Research & School of Energy Research, Xiamen University, Xiamen 361102, China. E-mail: pengzhang@xmu.edu.cn

† Electronic supplementary information (ESI) available. See DOI: 10.1039/d0qm00849d

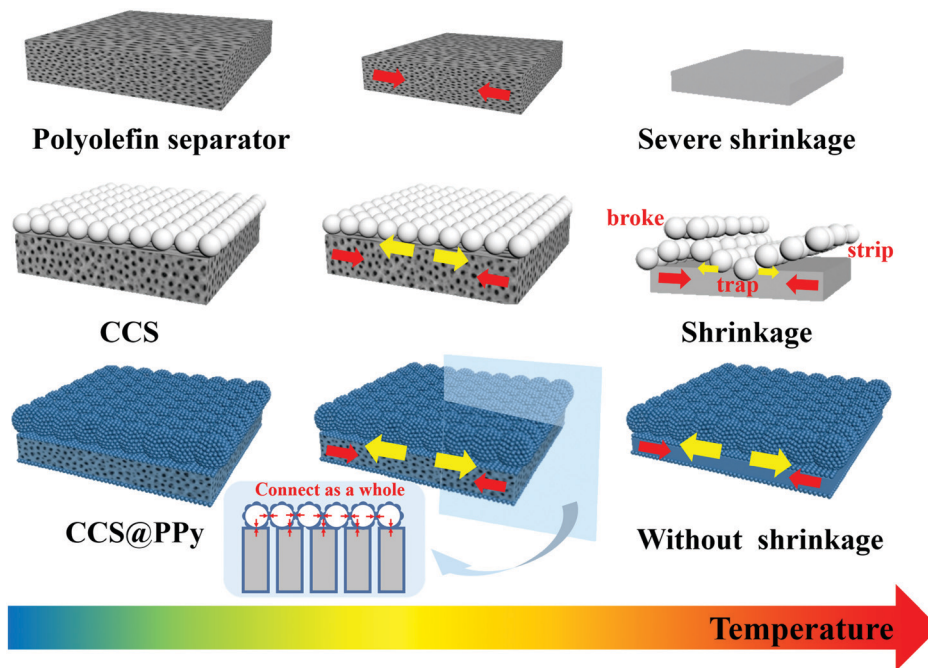


Fig. 1 Schematic of the failure of CCS and functional mechanism of CCS@PPy.

As a result, it will make the ceramic-coated layer fracture and even pill off from the polyolefin separator at an elevated temperature, losing the protective function of the ceramic coating layer. As shown in Fig. 1, the polyolefin separator melts at an elevated temperature. The interfacial incompatibility with the electrolyte makes it shut down micropores, and generate the tendency to shrink inward. After the modification of ceramic particles, the inherent inertia of ceramic particles has an opposite tendency to the shrinkage of the polyolefin membrane, thereby resisting the shrinkage of the polyolefin separator. Although the ceramic-coated layer has an effect on restraining the shrinkage of the separator, the ceramic-coated layer will break, trap and even strip from polyolefin separators when the binder melts with the increase of temperature, leading to the collapse of the ceramic-coated layer and the shrinkage of CCS.

Based on the above point of view, we developed a rational design of reinforced ceramic-coated separator, marked as CCS@PPy, by modifying the ceramic-coated separator with electron-insulated polypyrrole (PPy) throughout the entire separator. PPy is well known as a conductive polymer.<sup>30–33</sup> With the advantage of facile synthesis, it is widely used for the coating of materials by an *in situ* chemical oxidative polymerization reaction.<sup>30,31</sup> However, the eigenstate PPy without doping is virtually non-electron conductive since the valence electrons are difficult to transition from  $\pi$  to  $\pi^*$ .<sup>34,35</sup> In this work, we immerse commercial CCS in dilute pyrrole and ammonium persulfate solution at room temperature. Owing to the strong oxidizing property of ammonium persulfate (APS) and relatively high reaction temperature (compared to traditional chemical oxidation preparation of electron-conductive PPy in cold water bath), the backbone of PPy is partly oxidized

through free radical oxygen insertion and dopant degradation with the generation of C=O groups. The creation of C=O groups destroys the conjugated structure of PPy, resulting in the formation of electron-insulated PPy.<sup>36</sup>

By an *in situ* oxidation polymerization with APS as an oxidizing agent, the PPy forms an overall modified layer throughout the entire CCS. It then interconnects the ceramic particles and PE separator to a whole, as shown by the simplified cross-section schematic in Fig. 1. On the one hand, the PPy-modified layer improves the resistibility against the tendency of shrinkage by enhancing the adhesion, toughness and strength of the ceramic-coated layer. On the other hand, it decreases the shrinkage tendency by improving the interfacial compatibility with the electrolyte and physically restraining the shrinkage of the PE separator. Owing to the overall PPy-modified layer interconnecting the ceramic particles and PE separator as a whole matrix, the reinforced ceramic-coated layer is strong enough to retain its structural stability at higher temperature, preventing it from breaking up or even pilling off from the PE separator. Therefore, the thermal stability of the modified separator has a significant improvement. In addition, the compositions of the strong-polarity components, such as N element and C=O groups introduced by the PPy modification, improve the wettability of the separator, leading to a higher ionic conductivity and better rate capability of the LIBs.

## 2. Experimental section

### 2.1. Preparation of CCS@PPy

The ceramic-coated separator (20  $\mu\text{m}$  PE substrate layer with 3  $\mu\text{m}$   $\text{Al}_2\text{O}_3$  ceramic-coated layer, Jinhuigaoke, Guangdong,

China) was used as the modification substrate. CCS@PPy was prepared by immersing the CCS in various pyrrole concentrations (Py, Shanghai Macklin Biochemical Co., Ltd) and APS hybrid solution (Py:APS = 1:1, in molar) with the hybrid solvent of deionized water and ethanol (V:V = 1:1). After 10 h soakage at ambient temperature, the CCS turned black. The separator was then washed three times with the hybrid solvent. After drying at 60 °C for 24 h under vacuum conditions, the CCS@PPy was obtained. The CCS@PPy separators prepared by 7.5, 10, and 20 mmol L<sup>-1</sup> Py and APS hybrid solution were named as CCS@PPy-7.5, CCS@PPy-10, and CCS@PPy-20, respectively.

## 2.2. Electrode preparation and cell assembly

The positive electrodes were prepared by coating the slurry, containing 80 wt% LiFePO<sub>4</sub>, 10 wt% PVDF, 10 wt% acetylene black, on the aluminum foils, and *N*-methyl-pyrrolidine (NMP) was used as the solvent. The 2016-type coin half-cells were assembled to test the battery performances by sandwiching the separators between the LiFePO<sub>4</sub> positive electrodes and lithium-metal negative electrodes. The LB301 electrolyte containing 1 M LiPF<sub>6</sub> in ethylene carbonate (EC)/dimethyl carbonate (DMC) (1:1 volume, Zhangjiagang Guotaihuarong New Chemical Materials Co., Ltd) was chosen for the battery performance test. The cells were assembled in a glove box (M. Braun GmbH) with an argon atmosphere.

## 2.3. Characterizations and measurements

Fourier transform infrared spectroscopy (FT-IR, Nicolet IS5 spectrometer, Thermo Fisher Scientific Inc.) was used to analyze the chemical composition of the separators. The cross-section and surface morphologies of the separators were both measured by field emission scanning electron microscopy (FE-SEM, S-4800, Hitachi, Japan). The thickness of the PPy-coating layer was measured using a transmission electron microscope (TEM, Tecnai F30 TWIN, America). The thermal shrinkage rate ( $T_s$ ) of the separators was determined by cutting the separators into 2 cm × 2 cm squares, and measuring the areas after a 30 min constant-temperature treatment at various temperatures. The  $T_s$  was calculated according to the following equation:

$$T_s = (S_0 - S)/S_0 \times 100\%$$

where  $S_0$  and  $S$  denote the areas of the separators before and after the thermal shrinkage test. The adhesive force ( $F_a$ ) of the separators was measured by Universal Material Testing Machine (UTM-4000, SUNS, Shenzhen). One piece of separator was adhered between two stainless-steel moulds, and then the two stainless-steel moulds were pulled away to let the ceramic-coated layer peel from the PE separator (detailed schematic is shown in Fig. S4a, ESI<sup>†</sup>). The  $F_a$  was calculated using the following equation:

$$F_a = F/S$$

where  $F$  is the force of the ceramic-coated layer peeled from the PE separator, and  $S$  denotes the area of the separator adhered on steel sheets. The electrolyte uptake (EU) was tested by

measuring the weight of the separators before and after absorbing the liquid electrolyte, and was calculated by the following equation:

$$EU = (W - W_0)/W_0 \times 100\%$$

where  $W_0$  and  $W$  are the weight of the separators before and after absorbing the liquid electrolyte, respectively. The porosity ( $P$ ) of the separator was obtained by immersing the separator into *n*-butanol for around 10 min, and was calculated by the following equation:

$$P = (m - m_0)/(\rho \times V) \times 100\%$$

where  $m_0$  and  $m$  are the weight of the separators before and after absorbing *n*-butanol, respectively,  $V$  denotes the volume of the separators, and  $\rho$  denotes the density of *n*-butanol. The ionic conductivities of the separators were measured by assembled 2016-type coin cells with the separators sandwiched between two stainless-steel sheets, and using the electrochemical impedance spectra (EIS) technique on an electrochemical workstation (Solartron SI 1287) from 1 Hz to 100 kHz with 10 mV voltage amplitude. The ionic conductivities ( $\sigma$ ) of the separators were calculated using the equation, as follows:

$$\sigma = d/(R_b \times A)$$

where  $d$  represents the thickness of the separators,  $A$  represents the area of the stainless-steel sheets, and  $R_b$  means the bulk resistance, which was obtained by the fitting result of the Nyquist plots. The wettability of the separators was evaluated by a contact angle goniometer (Powereach JC2000C1, Shanghai Zhongchen Digital Technique Equipment Co., Ltd), and using the commercial LB-301 electrolyte as the test liquid. In order to investigate the shutdown function of the separators, the AC impedance measurement was conducted by an AutoLab working station with the temperature increasing from 90 °C to 200 °C at the rate of 1 °C min<sup>-1</sup>.

The cycle performance was tested using charge and discharge testers (LAND-V34, Wuhan LAND Electronics Co., Ltd) with a constant current-constant voltage (CC-CV) charge process and constant current discharge process in the voltage interval of 2.5–3.8 V at 0.5 C. The rate capability was tested by charging the cells at the same rate of 0.5 C, and discharging at various current densities of 0.5 C, 1.0 C, 2.0 C, 5.0 C and 10 C.

Li-Li symmetrical cells assembled with the separators were fabricated to measure the lithium ion transference number ( $t^+$ ). A voltage of 10 mV was used to polarize the cell. The  $t^+$  was calculated using the following equation:

$$t^+ = I_{ss} \times (\Delta V - I_0 \times R_0)/(I_0 \times (\Delta V - I_{ss} \times R_{ss}))$$

where  $R_0$  and  $R_{ss}$  were the resistance before and after polarization, respectively, obtained from AC impedance.  $I_0$  and  $I_{ss}$  were the initial current and steady current, respectively.

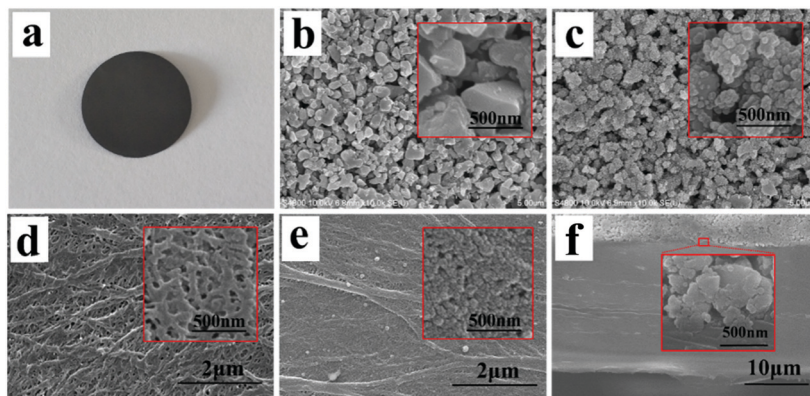


Fig. 2 (a) Photograph of the CCS@PPy-10 membrane, SEM images of the ceramic-coated side of the CCS (b) and CCS@PPy-10 membrane (c), SEM images of the uncoated side of CCS (d) and CCS@PPy-10 (e), SEM image of the cross-section of the CCS@PPy-10 membrane (f), and the insets show the enlarged images of each SEM image.

## 3. Results and discussion

### 3.1. Characterization

A photograph of the CCS@PPy-10 membrane is shown in Fig. 2a. The separator turns black after 10 hours immersion in the hybrid solution of Py and APS, which implies the successful generation of PPy through an *in situ* oxidation polymerization reaction.<sup>37,38</sup> The surface morphologies of CCS and CCS@PPy-10 are shown in Fig. 2b–e, and the enlarge images are provided. After the modification of PPy, the surface of CCS@PPy-10 turns rough and numerous PPy particles are coated on both sides of the separator. The SEM image of the cross-section of CCS@PPy-10 is shown in Fig. 2f, and the enlarged image shows the joint between the ceramic-coated layer and PE separator. As it shows, the PPy particles not only coat onto the surface of the CCS, but also permeate throughout the ceramic-coating layer, attaching the ceramic particles and PE separator together. The result implies that the PPy-coating layer can connect the ceramic-coated layer and PE separator to a whole, enhancing the adhesion, toughness and strength of the ceramic-coated layer. The thickness of the PPy-coating layer was measured using TEM by testing the PPy-modified Al<sub>2</sub>O<sub>3</sub> particles. As shown in Fig. S1 (ESI<sup>†</sup>), the thicknesses of the PPy-coating layer were around 20.4, 31.3, and 42.3 nm when the concentration of Py is 7.5, 10, and 20 mmol L<sup>-1</sup>.

To verify that the coating of PPy is electron-insulated, the electrical resistivity of PPy prepared by the same process as CCS@PPy was measured with multimeter, after compressing into a tablet under a pressure of 20 MPa. The result is shown in Table S1 (ESI<sup>†</sup>). The electrical resistivity of PPy was  $8.20 \times 10^9 \Omega \text{ cm}$  on average, which implied that the PPy synthesized in this condition is electron-insulated. For further explanation, the FT-IR spectra of PPy were carried out. As shown in Fig. 3, the band at  $3400 \text{ cm}^{-1}$  corresponds to the N–H stretching vibration, and the peak at  $1275 \text{ cm}^{-1}$  is the characteristic absorption band of the C–N bond. Both features are the characteristic absorption bands of PPy, and demonstrate the successful generation of PPy. However, an abnormal band appears at  $1701 \text{ cm}^{-1}$ , which can be attributed to the C=O stretching vibration. By looking up the

related references, it was found that this is due to polypyrrole backbone oxidation through free radical oxygen insertion and dopant degradation.<sup>36</sup> As shown in Fig. S2 (ESI<sup>†</sup>), PPy is degraded by OH radicals and generates C=O groups. The creation of C=O groups partly destroys the conjugated structure of PPy. Therefore, the PPy synthesized by this condition is electron-insulated.

The FT-IR analyses of CCS and CCS@PPy have also been carried out to confirm the successful modification of CCS with PPy. As shown in Fig. 3, for the CCS membrane, the peak at  $3456 \text{ cm}^{-1}$  corresponds to hydroxyl groups on the surface of the ceramic particles, and the band at  $1461 \text{ cm}^{-1}$  is attributed to the –CH<sub>2</sub>– bending vibration from the PE separator. In addition, a series of characteristic absorption bands, including  $1735 \text{ cm}^{-1}$ ,  $1250 \text{ cm}^{-1}$  and  $1066 \text{ cm}^{-1}$ , correspond to the carbonyl groups and C–O–C stretching vibration, which are due to the esters binder of the ceramic-coated separator. After the modification of PPy, CCS@PPy inherits most of the characteristic absorption bands from CCS and PPy, while two additional shifts can be discovered, as follows. The O–H and N–H stretching vibrations have a red shift to  $3360 \text{ cm}^{-1}$ , which is due to the formation of hydrogen bonds between O–H and N–H, reducing their electron cloud density. In addition, the generation of the hydrogen bond also leads to the increased electron cloud density of N element, resulting in a blue shift of the C–N stretching vibration from

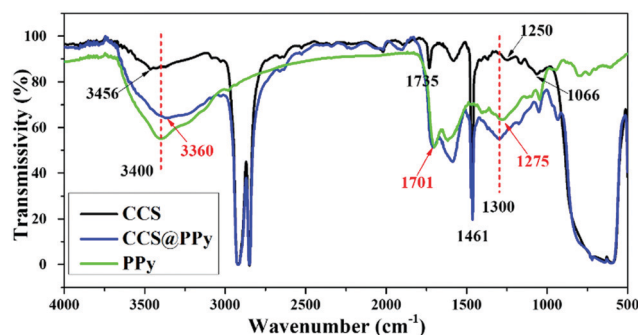


Fig. 3 FT-IR spectra of PPy, CCS and CCS@PPy.

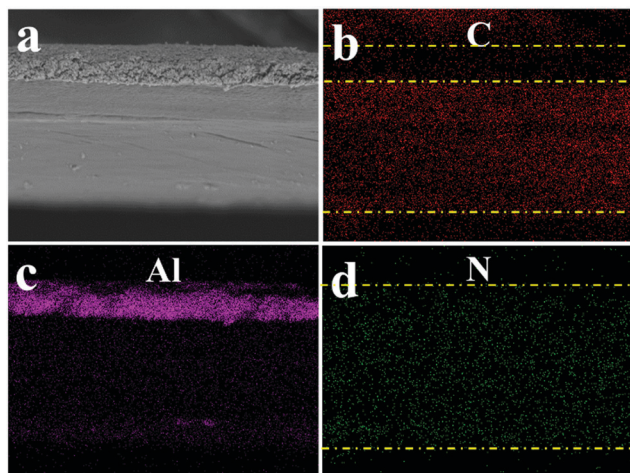


Fig. 4 The SEM image of the cross-section of CCS@PPy (a), and the elemental mapping of C, Al and N (b–d), respectively.

1275  $\text{cm}^{-1}$  to 1300  $\text{cm}^{-1}$ . Therefore, the FT-IR spectra have verified the successful generation of PPy on the CCS separator and the strong hydrogen bond interaction between PPy and ceramic particles. In addition, the strong interaction between PPy and ceramic particles can connect the ceramic particles to a whole, enhancing the toughness and mechanical strength of the ceramic-coated layer.

The EDX elemental mapping of the cross-section of CCS@PPy has been conducted to confirm the existence of PPy throughout the entire separator. As shown in Fig. 4, the distribution of the Al element corresponds with the area of the  $\text{Al}_2\text{O}_3$ -coated layer. The C element mainly distributes in the area of the PE layer, while the N element distributes evenly throughout the entire cross-section of CCS@PPy. It is worth noting that the distribution of the C element appears in the background area, which is due the influence of the C element in the conductive adhesive. However, the darker area between the PE layer and conductive adhesive, as marked in Fig. 4b, just corresponds with the area of the ceramic-coating layer. In addition, as for the N element, the signal in the area of the cross-section of CCS@PPy is much stronger than the signal in the background area, which further verifies the presence of N throughout the entire separator. Therefore, the EDX element analysis demonstrates that PPy not only coats onto the surface of the CCS, but also permeates throughout the entire separator to connect the ceramic-coated layer and PE layer as a whole. For further verification, the morphology of the inside PE layer was characterized by peeling off the ceramic layer and superficial PE layer. As shown in Fig. S3 (ESI<sup>+</sup>), the peeled CCS retains its original morphology (shown in Fig. 2d). As for CCS@PPy, there are numbers of weeny polypyrrole particles coated on the micropores of the PE separator. The result also demonstrates that PPy has permeated into the PE separator to form an overall-coating layer throughout the entire substrate separator after an *in situ* oxidation polymerization. In addition, the PPy-coating layer that permeated into the PE separator can decrease the shrinkage tendency by improving the interfacial compatibility

with electrolyte and physically restraining the shrinkage of the PE separator.

### 3.2. Safety performance of CCS@PPy

To verify the effectiveness of the PPy modification layer on improving the thermal stability of CCS, thermal shrinkage tests were carried out by measuring the area changes of the membranes at various temperatures for 30 min. As shown in Fig. 5a, both CCS and CCS@PPy-10 had no visible shrinkage at 130 °C. However, as the temperature went up, the CCS showed a large shrinkage of 25.0% at 150 °C and fragmented into powders at 200 °C, while CCS@PPy-10 had no visible shrinkage even up to 200 °C. To verify the mechanism of the improvement by the modification of PPy, SEM images of the separators after thermal shrinkage tests were obtained and are shown in Fig. 5b and c. The surface of CCS became wrinkled, and the ceramic-coated layer of CCS broke up and peeled off from the PE separator. The ceramic-coated layer thus lost its protective function for the PE separator, which corresponds to the failure mechanism of CCS, as shown in Fig. 1. However, the surface of CCS@PPy-10 was maintained evenly after heat treatment at 200 °C for 30 min. The reasons for this are as follows: (1) the overall PPy modification layer connected the ceramic particles and PE separator as a whole, and enhanced the adhesion of the ceramic-coated layer. As the result of the adhesion test shows in Fig. S4a (ESI<sup>+</sup>), both the breaking strength and displacement of CCS@PPy was improved. In addition, the image of CCS@PPy after the adhesion test is shown in Fig. S4b (ESI<sup>+</sup>). The color of the separator remained black after the ceramic-coated layer was peeled off, which also indicated that the PPy has permeated throughout the ceramic-coated layer to connect the ceramic-coated layer and PE separator as a whole, thereby improving the adhesion of CCS@PPy. (2) The hydrogen bond between PPy and ceramic particles improved the strength and toughness of the ceramic-coated layer. (3) The PPy that permeated into the PE separator decreased the shrinkage tendency by improving the interfacial compatibility with the electrolyte and physically restraining the

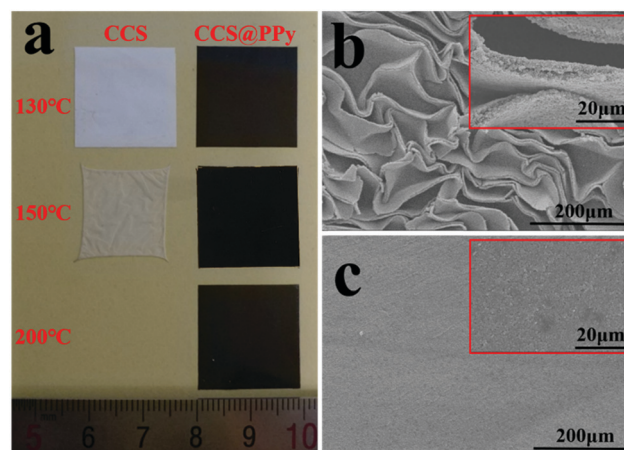


Fig. 5 (a) The image of CCS and CCS@PPy-10 after thermal shrinkage tests at 130 °C, 150 °C, and 200 °C for 30 min, respectively. SEM images of CCS (b) and CCS@PPy-10 (c) after the thermal shrinkage test.

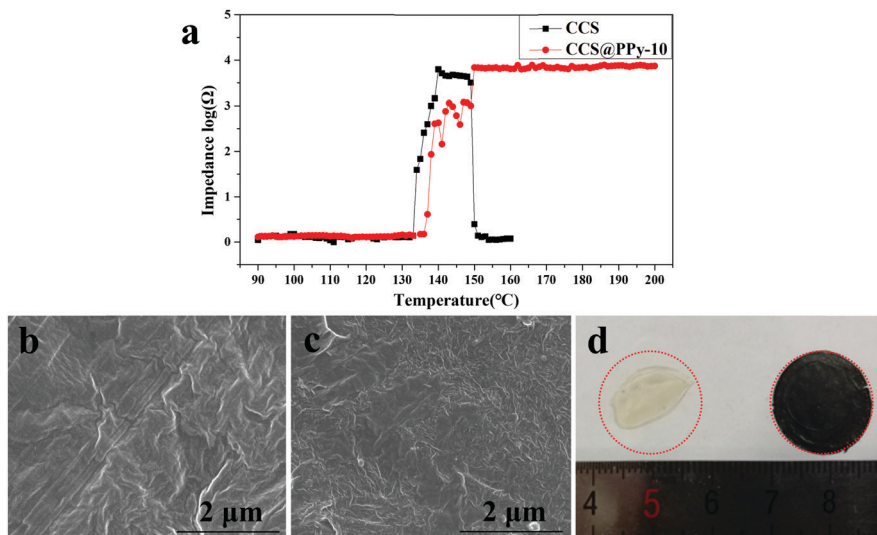


Fig. 6 (a) The resistance of CCS and CCS@PPy-10 with the function of temperature from 90 °C to 200 °C. SEM images of the PE side of CCS (b) and CCS@PPy-10 (c) after a heat treatment of 140 °C. (d) The image of CCS (left) and CCS@PPy-10 (right) after the shutdown function test.

shrinkage of PE separator. Therefore, the ceramic-coated layer of CCS@PPy can hold steady at a high temperature such that the thermal stability of CCS@PPy has a significant improvement. The thermal shrinkage test of the PE separator only modified with PPy (PE@PPy, prepared using 10 mmol L<sup>-1</sup> Py and APS hybrid solution) by the same process, was also conducted to demonstrate the necessity of the ceramic coated layer. As shown in Fig. S5 (ESI<sup>†</sup>), the PE separator showed a large shrinkage of 38.2% at 130 °C and became transparent with a larger shrinkage of 58.8% at 150 °C. After the modification of PPy, the thermal stability of PE@PPy does improve to have decreased shrinkages of 25.2% and 45.6% at 130 °C and 150 °C, respectively. This result indicated that the substantially improved thermal stability was due to the synergistic effect of the ceramic-coated layer and PPy. The PE separator only modified with PPy lacked sufficient rigidity to resist the shrinkage of the porous substrate separator at elevated temperature. Fig. S6 (ESI<sup>†</sup>) shows that CCS@PPy-7.5 has a large shrinkage after heating at 200 °C for 30 min, which demonstrates that the PPy-coating layer is too thin to resist the shrinkage of the separator.

The shutdown function is an effective way to prevent LIBs from thermal runaway. As the temperature goes up, the PE separator will melt at first and form a dense layer to shut down the ionic conduction. The ceramic-coated layer will then constantly maintain its dimensional stability to avoid the direct contact of the electrodes. This enables the synergistic function of the PE layer and ceramic-coated layer to prevent batteries from further thermal runaway.<sup>24,34,35</sup> The shutdown behavior can be investigated by electrochemical impedance measurement with the increase of temperature. The impedance changes of CCS and CCS@PPy-10 with the temperature increasing from 90 °C to 200 °C at the rate of 1 °C min<sup>-1</sup> are shown in Fig. 6a. The impedances of CCS and CCS@PPy-10 showed a leap at 134 °C and 137 °C, respectively. This was owing to the melt of the PE layer shutting down the micropores in the substrate separator

and effectively blocking the ionic channel between the electrodes. However, the impedance of CCS was rapidly reduced to almost 0 Ω at 150 °C. This indicated that CCS suffered from an obvious dimensional shrinkage, leading to the contact of the electrodes and an internal short circuit. On the contrary, the cell assembled with CCS@PPy-10 still kept an open circuit even at 200 °C. The effective temperature of the shutdown function for the CCS separator is only 130–150 °C. This has little effect to improve the safety performance of LIBs since the thermal inertia will make the temperature of the battery exceed the effective temperature. As for CCS@PPy-10, the effective temperature of the shutdown function is 137–200 °C, which provides a sufficient buffer space for thermal inertia. Therefore, CCS@PPy-10 shows a better safety performance to prevent batteries from further runaway at high temperature. For further verification, SEM images are shown in Fig. 6b and c of the PE side of CCS and CCS@PPy-10 after a heat treatment of 140 °C for 30 min, respectively. The micropores of both separators disappeared with the melt of the PE layer. This indicated that the PE layer has formed a dense layer to shut down the ionic conduction at elevated temperature. The photographs of the membranes after the shutdown function test are shown in Fig. 6d. The CCS showed a large shrinkage, leading to the contact of the electrodes and internal short circuit. On the contrary, with significantly improved thermal stability by the overall-covered PPy modification layer, CCS@PPy-10 maintained its original integrity to keep preventing the contact of the electrodes. These results were consistent with the shutdown behavior of CCS and CCS@PPy-10.

The mechanical property of the separator is also very vital to ensure the safety of the LIBs. Fig. S7a (ESI<sup>†</sup>) shows that the mechanical strength of CCS@PPy has a distinct improvement since the overall-covered PPy-coating layer connects the PE separator and ceramic-coating layer as a whole. Fig. S7b (ESI<sup>†</sup>) also shows that the CCS@PPy has a good flexibility to meet the requirement of the battery assembly.

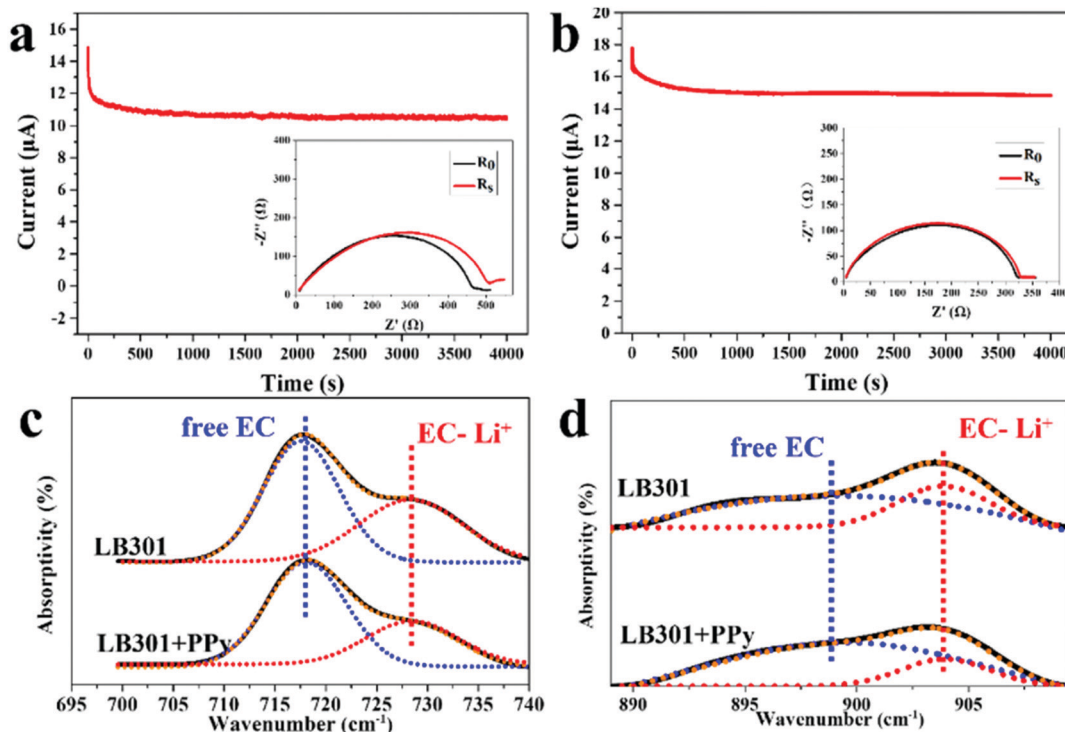


Fig. 7 The lithium ion transference number plot of CCS (a) and CCS@PPy-10 (b), FT-IR spectra (solid lines) and the constituting peaks obtained after spectrum deconvolution (dotted lines) in the 700–740  $\text{cm}^{-1}$  (c) and 890–910  $\text{cm}^{-1}$  ranges (d).

### 3.3. Electrochemical performances

A high  $t^+$  is beneficial to obtain a higher rate capability, lower concentration polarization, and slow down Li dendrite nucleation.<sup>39–42</sup> The  $t^+$  was measured by the steady current method with a 10 mV potential polarization. The results are shown in Fig. 7a and b. The  $t^+$  of CCS@PPy-10 improved largely from 0.35 to 0.56, after the modification of PPy. To further understand the function of the PPy for improving  $t^+$ , the FT-IR tests of the commercial electrolyte (LB301) and LB301 with the addition of PPy were each carried out. It is worth noting that the characteristic absorption bands of PPy have been deduced by background scanning. As shown in Fig. 7c and d, the characteristic peaks of the ring bending modes of free EC and  $\text{Li}^+$ -associated EC (EC- $\text{Li}^+$ ) were identified at 717.8  $\text{cm}^{-1}$  and 728.2  $\text{cm}^{-1}$ , respectively. Furthermore, the symmetric ring breathing modes of free EC and EC- $\text{Li}^+$  were identified at 899.1  $\text{cm}^{-1}$  and 904.3  $\text{cm}^{-1}$ , respectively.<sup>43</sup> In a high dielectric constant solvent, the  $\text{Li}^+$  ions preferred to be surrounded with solvent molecules, rather than anions, so that the mobility of the  $\text{Li}^+$  ions was greatly constrained since the formation of larger EC- $\text{Li}^+$  complexes. It was noteworthy that with the addition of PPy, LB301 showed a significantly suppressed relative signal of EC- $\text{Li}^+$  to free EC molecules, which indicated the decreased interaction of the EC molecules with the  $\text{Li}^+$  ions. In this case, the size of the EC- $\text{Li}^+$  complex decreased, which was beneficial to improve the mobility of  $\text{Li}^+$ . Therefore, the  $\text{Li}^+$  ion transference number of the cell assembled with CCS@PPy-10 improved.

It is one of the functions of separators to provide ion conduction by absorbing the electrolyte, and the more electrolyte absorbed in

the separator, the higher the ion conductivity will be.<sup>44–46</sup> The electrolyte uptake is mainly affected by the porosity and wettability of the separator. However, in consideration of safety, the porosity of the separators is usually limited to be 40–50%. Owing to the nonpolarity of the polyolefin separators, the separators show poor wettability with strong-polar liquid electrolytes, which will not only prolong the time for assembly in battery manufacturing processes, but also result in poor battery performance. The contact angles of the separators were carried out to evaluate the wettability of the

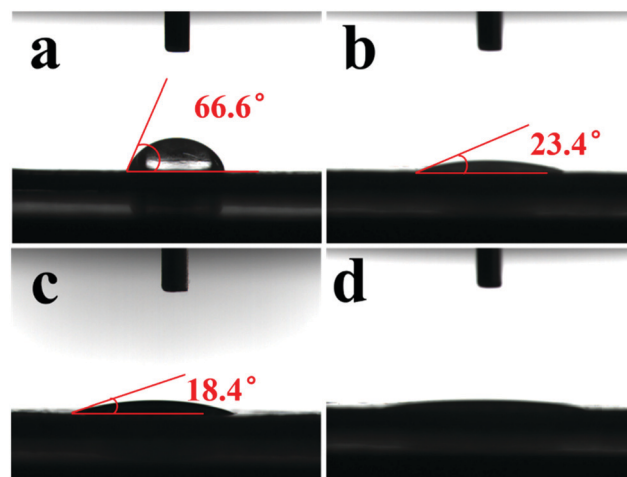


Fig. 8 Contact angle images of PE separator (a), ceramic-coated side of CCS (b), PE side of CCS@PPy-10 (c) and ceramic-coated side of CCS@PPy-10 (d).

**Table 1** Physical properties of the PE, CCS and CCS@PPy separator

Separator	PE separator	CCS	CCS@PPy-7.5	CCS@PPy-10	CCS@PPy-20
Thickness ( $\mu\text{m}$ )	20	23	23	23	23
Porosity (%)	44.2	47.8	44.7	43.5	40.4
Electrolyte uptake (%)	56	82	78	75	61
Ion conductivity ( $\text{mS cm}^{-1}$ )	0.54	0.67	0.66	0.61	0.29

separators with the commercial liquid electrolyte. As shown in Fig. 8a–d, the electrolyte wettability of the PE separator is poor with a large contact angle of  $66.0^\circ$ . After the coating of the ceramic particles, the contact angle of CCS decreases largely to  $23.4^\circ$ . As for CCS@PPy-10, the wettability on both sides of the separator has a distinct improvement. The contact angle of the PE side decreases from  $66.0^\circ$  to  $18.4^\circ$ , and the ceramic-coated side reduces significantly to near zero. This result implies that the modification of PPy can significantly enhance the wettability of the separator because of the strong-polarity components of PPy, such as N element and C=O groups. In addition, PPy not only improves the superficial wettability, but also ameliorates the integral wettability of the separator by the overall-covered modification layer throughout the entire substrate membrane.

Several physical properties of the PE separator, CCS and CCS@PPy are listed in Table 1. The thickness of CCS@PPy has no visible increase compared to CCS, which is beneficial to retain the high energy density of LIBs. The porosity of the PE separator is 44.2%, and CCS has a larger porosity of 47.8%.

After the modification of PPy, the CCS@PPy-7.5, CCS@PPy-10, and CCS@PPy-20 show lower porosity values of 44.7%, 43.5% and 40.4%, respectively. Obviously, the reason for this could be that the PPy modification layer occupies parts of the interspace of CCS, and decreases the porosity. Although modification of PPy slightly reduces the porosity, the excellent wettability promotes it to absorb more electrolyte. As result, the electrolyte uptake of CCS@PPy-7.5 and CCS@PPy-10 increases from 56% to 78% and 75%, compared to the PE separator. However, as for CCS@PPy-20, the excessive PPy-coating layer blocks the micropores in the separator, resulting in a much lower electrolyte uptake of 61%.

The ionic conductivity values of CCS@PPy-7.5, CCS@PPy-10, and CCS@PPy-20 are 0.66, 0.61, and  $0.29 \text{ mS cm}^{-1}$ , respectively, obtained according to the electrochemical impedance spectroscopy shown in Fig. S8 (ESI<sup>†</sup>). The result demonstrates that the immoderate PPy-coating layer obstructs the ionic transportation, leading to the deterioration of the electrochemical performance. The CCS@PPy-10 is the optimum-modified separator that has excellent thermal stability, as well as ionic conductivity.

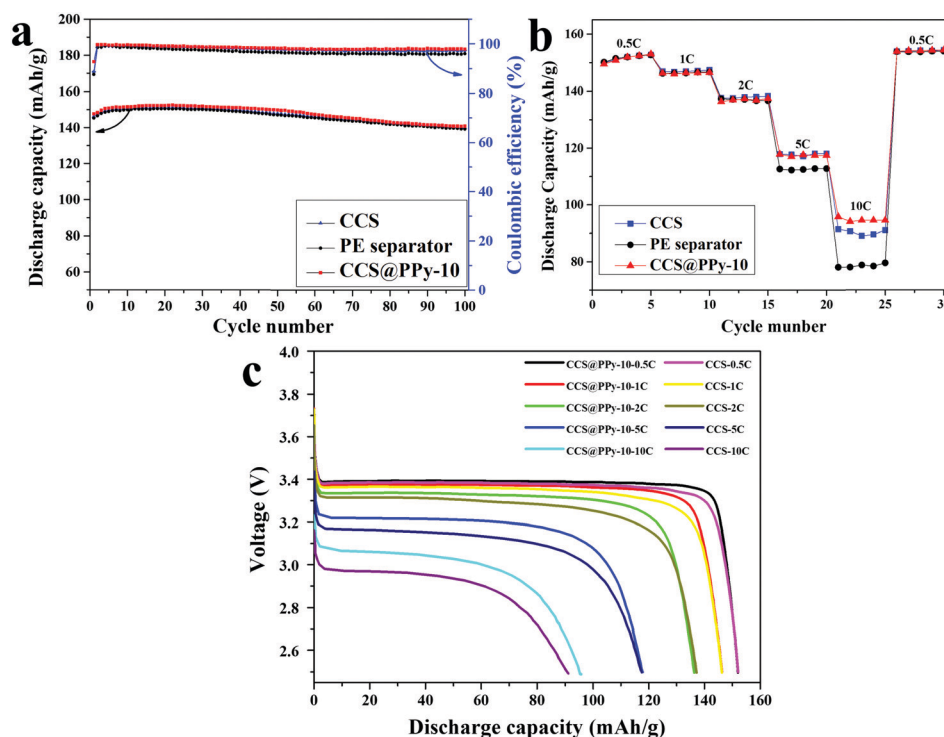


**Fig. 9** (a) The cycle performance of the  $\text{LiFePO}_4/\text{Li}$  cells assembled with the PE separator, CCS and CCS@PPy-10 at 0.5 C, respectively. (b) The rate performances of  $\text{LiFePO}_4/\text{Li}$  half-cells assembled with a commercial PE separator, CCS and CCS@PPy-10 at 0.5 C, 1 C, 2 C, 5 C and 10 C, respectively. (c) The discharge curves of CCS and CCS@PPy-10 at various rates.



The cycle performance of the cells assembled with a PE separator, CCS and CCS@PPy-10 have been investigated by LiFePO<sub>4</sub>/Li half-cells at 0.5 C under the potential range from 2.5 V to 3.8 V. As shown in Fig. 9a, after 100 cycles operated at the rate of 0.5 C, the cells assembled with the PE separator, CCS and CCS@PPy-10 remained at 93.6%, 93.5% and 93.5% of their original discharge capacities, respectively. In addition, all three kinds of separators remained at high Coulombic efficiency above 98%. The results demonstrated that the modifications of PPy and the ceramic particles had no negative impact on the battery performance.

The rate capability performance of the three kinds of separators has also been investigated at the rates of 0.5 C, 1 C, 2 C, 5 C, and 10 C, and finally returns to 0.5 C. As shown in Fig. 9b, the rate capabilities of all three kinds of separators had a similar discharge capacity at the rates of 0.5 C, 1 C, and 2 C. With the increase of the current rate, the PE separator showed lower capacity retentions of 73.2% and 51.7% at 5 C and 10 C, respectively. By comparison, both of the cells assembled with CCS and CCS@PPy-10 showed improved capacity retentions of 77.4%, 77.5% at 5 C, and 59.2%, 62.1% at 10 C, respectively. These results were consistent with the results of the ionic conductivity. At relatively low rates, the ionic conductivity was high enough to meet the demand of the Li<sup>+</sup> ion for the electrodes, such that all of the separators showed a similar performance at the current rates under 2 C. However, at a relatively high current rate, the ionic conductivity became one of the determining factors, so the cells assembled with CCS and CCS@PPy-10 exhibited better rate performance. LIB is developed based on the principle of lithium ion intercalation and deintercalation on a negative electrode and positive electrode. Therefore, the transportation of the Li<sup>+</sup> ion rather than the anion is effective when a battery works. Although the ionic conductivity of CCS@PPy-10 was lower than that of CCS, the real Li<sup>+</sup> ion conductivity of CCS@PPy-10 (0.34 mS cm<sup>-1</sup>) was higher than CCS (0.23 mS cm<sup>-1</sup>) since it had a higher  $t^+$ . Thus, the cells assembled with CCS@PPy-10 showed a better rate capacity. For more details, the discharge curves of CCS and CCS@PPy-10 at various rates are shown in Fig. 9c. The cells assembled with CCS@PPy-10 had a relatively lower polarization voltage, especially at 5 C and 10 C. This is because the cell assembled with CCS@PPy-10 had a higher  $t^+$ , leading to the reduction of the concentration polarization. As we know, the energy is a product of the voltage, current and time. The lower polarization voltage can achieve a higher discharge platform, thereby obtaining more energy.

## 4. Conclusions

In summary, a rational design of the reinforced ceramic-coated separator is proposed by modifying the ceramic-coated separator with an overall-covered layer of electron-insulated PPy throughout the entire separator. On the one hand, the overall-covered PPy modification layer improves resistibility against the tendency of shrinkage by enhancing the adhesion, toughness and strength of the ceramic-coated layer. On the other hand, it decreases the

shrinkage tendency by improving the interfacial compatibility with the electrolyte and physically restraining the shrinkage of the PE separator. Therefore, the modified separator shows an improved thermal dimensional stability without visible shrinkage at 200 °C. Owing to the higher Li<sup>+</sup> transference number and better electrolyte wettability, the cell assembled with CCS@PPy shows a lower polarization voltage and better rate capacity. With the synergistic function of the PE layer, ceramic-coated layer and PPy modification layer, the CCS@PPy exhibits a wider temperature range of thermal shutdown function from 137 °C to 200 °C, preventing the batteries from further thermal runaway at high temperatures. Considering the rapid development of new energy-powered vehicles, this rational design of reinforced ceramic-coated separator will be very promising for industrialization to guarantee their safety performance.

## Conflicts of interest

There are no conflicts to declare.

## Acknowledgements

We gratefully acknowledge the financial support from the National Natural Science Foundation of China (21875198 and 21875195), National Key Research and Development Program of China (2017YFB0102000), Fundamental Research Funds for the Central Universities (20720190040), and the Key Project of Science and Technology of Fujian Province (2018H6019).

## Notes and references

- 1 K. H. Park, Q. Bai, D. H. Kim, D. Y. Oh, Y. Zhu, Y. Mo and Y. S. Jung, Design Strategies, Practical Considerations, and New Solution Processes of Sulfide Solid Electrolytes for All-Solid-State Batteries, *Adv. Energy Mater.*, 2018, **8**, 1800035.
- 2 J. Liu, H. Nara, T. Yokoshima, T. Momma and T. Osaka, Li<sub>2</sub>S cathode modified with polyvinylpyrrolidone and mechanical milling with carbon, *J. Power Sources*, 2015, **273**, 1136–1141.
- 3 D. Ren, X. Liu, X. Feng, L. Lu, M. Ouyang, J. Li and X. He, Model-based thermal runaway prediction of lithium-ion batteries from kinetics analysis of cell components, *Appl. Energy*, 2018, **228**, 633–644.
- 4 X. Zhang, E. Sahraei and K. Wang, Li-ion Battery Separators, Mechanical Integrity and Failure Mechanisms Leading to Soft and Hard Internal Shorts, *Sci. Rep.*, 2016, **6**, 32578.
- 5 X. N. Feng, D. S. Ren, X. M. He and M. G. Ouyang, Mitigating Thermal Runaway of Lithium-Ion Batteries, *Joule*, 2020, **4**, 743–770.
- 6 F. Jiang, Y. Nie, L. Yin, Y. Feng, Q. Yu and C. Zhong, Core-shell-structured nanofibrous membrane as advanced separator for lithium-ion batteries, *J. Membr. Sci.*, 2016, **510**, 1–9.
- 7 C. Liu, H. Li, X. Kong and J. Zhao, Modeling analysis of the effect of battery design on internal short circuit hazard in LiNi<sub>0.8</sub>Co<sub>0.1</sub>Mn<sub>0.1</sub>O<sub>2</sub>/SiO<sub>x</sub>-graphite lithium ion batteries, *Int. J. Heat Mass Transfer*, 2020, **153**, 119590.

- 8 X. S. Huang and J. Hitt, Lithium ion battery separators: Development and performance characterization of a composite membrane, *J. Membr. Sci.*, 2013, **425**, 163–168.
- 9 P. Yang, P. Zhang, C. Shi, L. Chen, J. Dai and J. Zhao, The functional separator coated with core-shell structured silica-poly(methyl methacrylate) sub-microspheres for lithium-ion batteries, *J. Membr. Sci.*, 2015, **474**, 148–155.
- 10 H. Li, C. Liu, X. Kong, J. Cheng and J. Zhao, Prediction of the heavy charging current effect on nickel-rich/silicon-graphite power batteries based on adiabatic rate calorimetry measurement, *J. Power Sources*, 2019, **438**, 226971.
- 11 C. Shi, J. Dai, X. Shen, L. Peng, C. Li, X. Wang, P. Zhang and J. Zhao, A high-temperature stable ceramic-coated separator prepared with polyimide binder/Al<sub>2</sub>O<sub>3</sub> particles for lithium-ion batteries, *J. Membr. Sci.*, 2016, **517**, 91–99.
- 12 D. Takemura, S. Aihara, K. Hamano, M. Kise, T. Nishimura, H. Urushibata and H. Yoshiyasu, A powder particle size effect on ceramic powder based separator for lithium rechargeable battery, *J. Power Sources*, 2005, **146**, 779–783.
- 13 D. Li, D. Shi, Z. Yuan, K. Feng, H. Zhang and X. Li, A low cost shutdown sandwich-like composite membrane with superior thermo-stability for lithium-ion battery, *J. Membr. Sci.*, 2017, **542**, 1–7.
- 14 L. Xia, L. Yu, D. Hu and G. Z. Chen, Electrolytes for electrochemical energy storage, *Mater. Chem. Front.*, 2017, **1**, 584–618.
- 15 H. Li, D. Wu, J. Wu, L. Y. Dong, Y. J. Zhu and X. Hu, Flexible, High-Wettability and Fire-Resistant Separators Based on Hydroxyapatite Nanowires for Advanced Lithium-Ion Batteries, *Adv. Mater.*, 2017, **29**.
- 16 N. Angulakshmi, R. B. Dhanalakshmi, M. Kathiresan, Y. Zhou and A. M. Stephan, The suppression of lithium dendrites by a triazine-based porous organic polymer-laden PEO-based electrolyte and its application for all-solid-state lithium batteries, *Mater. Chem. Front.*, 2020, **4**, 933–940.
- 17 D. Yang, L. He, Y. Liu, W. Yan, S. Liang, Y. Zhu, L. Fu, Y. Chen and Y. Wu, An acetylene black modified gel polymer electrolyte for high-performance lithium-sulfur batteries, *J. Mater. Chem. A*, 2019, **7**, 13679–13686.
- 18 S. Liang, Y. Shi, T. Ma, W. Yan, S. Qin, Y. Wang, Y. Zhu, H. Wang and Y. Wu, A Compact Gel Membrane Based on a Blend of PEO and PVDF for Dendrite-Free Lithium Metal Anodes, *ChemElectroChem*, 2019, **6**, 5413–5419.
- 19 Y. Liu, D. Yang, W. Yan, Q. Huang, Y. Zhu, L. Fu and Y. Wu, Synergy of Sulfur/Polyacrylonitrile Composite and Gel Polymer Electrolyte Promises Heat-Resistant Lithium-Sulfur Batteries, *iScience*, 2019, **19**, 316–325.
- 20 W. Zhang, J. Nie, F. Li, Z. L. Wang and C. Sun, A durable and safe solid-state lithium battery with a hybrid electrolyte membrane, *Nano Energy*, 2018, **45**, 413–419.
- 21 Y. L. Liu, Chao Li, Bojie Song, Hucheng Cheng, Zhu Chen, Minrui He and Ping Zhou, Haoshen, Germanium Thin Film Protected Lithium Aluminum Germanium Phosphate for Solid-State Li Batteries, *Adv. Energy Mater.*, 2018, 1702374.
- 22 Y. Ding, X. Shen, J. Zeng, X. Wang, L. Peng, P. Zhang and J. Zhao, Pre-irradiation grafted single lithium-ion conducting polymer electrolyte based on poly(vinylidene fluoride), *Solid State Ionics*, 2018, **323**, 16–24.
- 23 P.-Y. Ji, J. Fang, Y.-Y. Zhang, P. Zhang and J.-B. Zhao, Novel Single Lithium-Ion Conducting Polymer Electrolyte Based on Poly(hexafluorobutyl methacrylate-co-lithium allyl sulfonate) for Lithium-Ion Batteries, *ChemElectroChem*, 2017, **4**, 2352–2358.
- 24 S. Wang, X. Liu, A. Wang, Z. Wang, J. Chen, Q. Zeng, X. Wang and L. Zhang, An ionic liquid crystal-based solid polymer electrolyte with desirable ion-conducting channels for superior performance ambient-temperature lithium batteries, *Polym. Chem.*, 2018, **9**, 4674–4682.
- 25 C. Zuo, B. Zhou, Y. H. Jo, S. Li, G. Chen, S. Li, W. Luo, D. He, X. Zhou and Z. Xue, Facile fabrication of a hybrid polymer electrolyte via initiator-free thiol-ene photopolymerization for high-performance all-solid-state lithium metal batteries, *Polym. Chem.*, 2020, **11**, 2732–2739.
- 26 J. Dai, C. Shi, C. Li, X. Shen, L. Peng, D. Wu, D. Sun, P. Zhang and J. Zhao, A rational design of separator with substantially enhanced thermal features for lithium-ion batteries by the polydopamine-ceramic composite modification of polyolefin membranes, *Energy Environ. Sci.*, 2016, **9**, 3252–3261.
- 27 C. Shi, J. Dai, C. Li, X. Shen, L. Peng, P. Zhang, D. Wu, D. Sun and J. Zhao, A Modified Ceramic-Coating Separator with High-Temperature Stability for Lithium-Ion Battery, *Polymers*, 2017, **9**, 159.
- 28 C. Shi, P. Zhang, L. Chen, P. Yang and J. Zhao, Effect of a thin ceramic-coating layer on thermal and electrochemical properties of polyethylene separator for lithium-ion batteries, *J. Power Sources*, 2014, **270**, 547–553.
- 29 L. Peng, X. Shen, J. Dai, X. Wang, J. Zeng, B. Huang, H. Li, P. Zhang and J. Zhao, Three-Dimensional Coating Layer Modified Polyolefin Ceramic-Coated Separators to Enhance the Safety Performance of Lithium-Ion Batteries, *J. Electrochem. Soc.*, 2019, **166**, A2111–A2120.
- 30 M. F. Attia, N. Anton, I. U. Khan, C. A. Serra, N. Messaddeq, A. Jakhmola, R. Vecchione and T. Vandamme, One-step synthesis of iron oxide polypyrrole nanoparticles encapsulating ketoprofen as model of hydrophobic drug, *Int. J. Pharm.*, 2016, **508**, 61–70.
- 31 A. Chatterjee and S. Maity, A comparative study of reaction kinetics of *in situ* chemical polymerization of polypyrrole onto various textile fibres, *Surf. Coat. Technol.*, 2017, **324**, 569–576.
- 32 G. Wan, L. Yang, S. Shi, Y. Tang, X. Xu and G. Wang, Ti<sub>2</sub>Nb<sub>10</sub>O<sub>29</sub> microspheres coated with ultrathin N-doped carbon layers by atomic layer deposition for enhanced lithium storage, *Chem. Commun.*, 2019, **55**, 517–520.
- 33 G. Ruhi, O. P. Modi and S. K. Dhawan, Chitosan-polypyrrole-SiO<sub>2</sub> composite coatings with advanced anticorrosive properties, *Synth. Met.*, 2015, **200**, 24–39.
- 34 T. O. Shinichi, Komaba a Impedance analysis of electro-deposited insulating polypyrrole, *J. Electroanal. Chem.*, 1998, **453**, 5.
- 35 P. Pfluger, M. Krounbi, G. B. Street and G. Weiser, The chemical and physical properties of pyrrole – based conducting polymers: The oxidation of neutral polypyrrole, *J. Chem. Phys.*, 1983, **78**, 3212–3218.

- 36 R. Buitrago-Sierra, M. J. García-Fernández, M. M. Pastor-Blas and A. Sepúlveda-Escribano, Environmentally friendly reduction of a platinum catalyst precursor supported on polypyrrole, *Green Chem.*, 2013, **15**, 1981.
- 37 X. Zhang, X. Yan, J. Guo, Z. Liu, D. Jiang, Q. He, H. Wei, H. Gu, H. A. Colorado, X. Zhang, S. Wei and Z. Guo, Polypyrrole doped epoxy resin nanocomposites with enhanced mechanical properties and reduced flammability, *J. Mater. Chem. C*, 2015, **3**, 162–176.
- 38 Z. Huang, H. Pan, W. Yang, H. Zhou, N. Gao, C. Fu, S. Li, H. Li and Y. Kuang, In Situ Self-Template Synthesis of Fe-N-Doped Double-Shelled Hollow Carbon Microspheres for Oxygen Reduction Reaction, *ACS Nano*, 2018, **12**, 208–216.
- 39 J. Zhang, L. Yue, Q. Kong, Z. Liu, X. Zhou, C. Zhang, Q. Xu, B. Zhang, G. Ding, B. Qin, Y. Duan, Q. Wang, J. Yao, G. Cui and L. Chen, Sustainable, heat-resistant and flame-retardant cellulose-based composite separator for high-performance lithium ion battery, *Sci. Rep.*, 2014, **4**, 3935.
- 40 L. Zhang, S. Wang, J. Li, X. Liu, P. Chen, T. Zhao and L. Zhang, A nitrogen-containing all-solid-state hyperbranched polymer electrolyte for superior performance lithium batteries, *J. Mater. Chem. A*, 2019, **7**, 6801–6808.
- 41 K. M. Diederichsen, E. J. McShane and B. D. McCloskey, Promising Routes to a High  $\text{Li}^+$  Transference Number Electrolyte for Lithium Ion Batteries, *ACS Energy Lett.*, 2017, **2**, 2563–2575.
- 42 H. Zhang, C. Li, M. Piszcz, E. Coya, T. Rojo, L. M. Rodríguez-Martinez, M. Armand and Z. Zhou, Single lithium-ion conducting solid polymer electrolytes: advances and perspectives, *Chem. Soc. Rev.*, 2017, **46**, 797–815.
- 43 M. Chi, L. Shi, Z. Wang, J. Zhu, X. Mao, Y. Zhao, M. Zhang, L. Sun and S. Yuan, Excellent rate capability and cycle life of Li metal batteries with  $\text{ZrO}_2/\text{POSS}$  multilayer-assembled PE separators, *Nano Energy*, 2016, **28**, 1–11.
- 44 K. Xu, Electrolytes and interphases in Li-ion batteries and beyond, *Chem. Rev.*, 2014, **114**, 11503–11618.
- 45 W. Lu, Z. Yuan, Y. Zhao, H. Zhang, H. Zhang and X. Li, Porous membranes in secondary battery technologies, *Chem. Soc. Rev.*, 2017, **46**, 2199–2236.
- 46 S. Qin, Y. Wang, X. Wu, X. Zhang, Y. Zhu, N. Yu, Y. Zhang and Y. Wu, Nylon-Based Composite Gel Membrane Fabricated via Sequential Layer-by-Layer Electrospinning for Rechargeable Lithium Batteries with High Performance, *Polymers*, 2020, **12**, 1572–1583.